High-resolution tomographic imaging of vacuum magnetic surfaces in the H-1 heliac

B. D. Blackwell, R. B. Tumlos, and J. Howard
Plasma Research Laboratory, Research School of Physical Sciences and Engineering, The Australian National University, Canberra, Australia

(Presented on 13 May 1996)

A new, high-precision rotating wire grid apparatus for vacuum magnetic surface mapping of current-free toroidal plasma confinement geometries is described. This full-scaled version of the prototype apparatus[1] developed on the SHEILA heliac has been tested and permanently installed on the H-1 heliac. Data of high quality are obtained with low electron energy (<20 eV) to avoid drift errors, with submillimeter resolution and accuracy, within a 700 mm circular field of view. The apparatus avoids pixcell resolution limits and optical distortion, and is shown to be highly suited to precise comparison of computed and experimental magnetic surfaces, and after tomographic inversion, can produce useful images of the magnetic surfaces. © *1997 American Institute of Physics.* [S0034-6748(97)72501-2]

I. INTRODUCTION

One of the chief reasons for the recent progress in advanced magnetic confinement configurations has been the experimental mapping of the magnetic field lines, from straightforward probing methods[2] to sophisticated imaging techniques, using fluorescent mesh or rod targets and optical image acquisition.[3–6] The apparatus described here combines the best of both techniques, directly collecting electrons using a wire array and producing images by tomographic inversion. Electrons from a small electron gun are collected by a grid of tautly stretched, parallel fine wires which is rotated in small steps to scan the cross section. Low energy (<20 eV) electrons are used to avoid curvature drift effects, the system is free of any optical imaging distortion, and is not limited in resolution by pixel size or mesh spacings. Time dependent data are available for dynamic analysis, or the system can be quickly scanned to give a complete profile. Rapid modulation of the beam intensity or position can provide transit sequence information, from which accurate values of rotational transform can be calculated.

The H-1 heliac [$R/a=1$ m/0.2 m, $B_0=0.2$ T (cont.) to 1 T][7] is a helical axis stellarator capable of a very wide range of low-shear, high-transform-per period $0.6 < \iota\!\!- < 2$, closed flux configurations with magnetic wells of both signs (+5% to −2%). It is particularly important for such new magnetic configurations that the surfaces are well characterized and possible sources of magnetic field error are investigated.

II. APPARATUS

The rotating grid (Fig. 1) is of an array of 64 molybdenum wires (0.15 mm diam, 4 mm spacing) stretched across a precisely rotating carrier ring, and insulated at both ends. The main mechanical design criteria were precision, and that the apparatus be available for use whenever required. The precision criterion was met by striving for high accuracy, but more importantly ensuring that motion was reproducible so that various calibration systems could maintain accuracy. Mounting the apparatus permanently in the machine, occupying minimal port space, providing a method of ''parking'' the wheel protected from the plasma, and avoiding any special surface coatings that might deteriorate (e.g., fluorescent powder) allows the apparatus to be ready for operation with only a few hours of preparation and calibration.

The design is based on the inherent accuracy of rotary motion, enhanced by two improvements over the prototype—the use of some kinematic design principles in the rotating bearing, and careful attention to wire tension. A central bearing is ruled out by the need of about 360° of rotation without obstruction of the plasma by radial support members—at least 180° for the tomographic data, and the same again to remove the wire grid from the plasma. The main problem in the prototype was that the rotating carrier, overconstrained by its outside bearing, would distort very slightly during rotation, and this would have a greatly magnified effect on the wire positions if they became even slightly slack. The present design uses four ball bearings running in a *V* groove inside the (outer) support ring, thus requiring that only the support ring be perfectly circular, and that the four ball bearing mounts be adjusted to lie on a circular arc. Although quite thick ($780\phi \times 25 \times 25$ mm SS316), the flexibility of the rotating ring requires more than the kinematically desirable two ball bearing support points. So that the rotating ring did not need to be made perfectly circular over its entire circumference, the bearings are constrained to operate in sliding friction with teflon pads on the rotating ring, but allowed to roll in the *V* groove. This combination of rolling and sliding friction is critical.

In this way, changes in dimensions of the ring as it rotates are kept below ±0.7 mm, and the wires are pretensioned so that they are stretched by more than this amount (up to 1.2 mm). This is accomplished by adjusting the transverse vibrational resonant frequency of the wires to the values required by the various lengths and tensions. The frequency is measured by grounding the free end of the plucked wire, and monitoring the small oscillating voltage produced in a weak magnetic field (0.01 T). The resonant frequencies are spread from 80 to 95 Hz, and adjusted to avoid harmonics of the mains frequency 50 Hz, and submultiples of the turbo-molecular pump rotation speed (600 Hz).

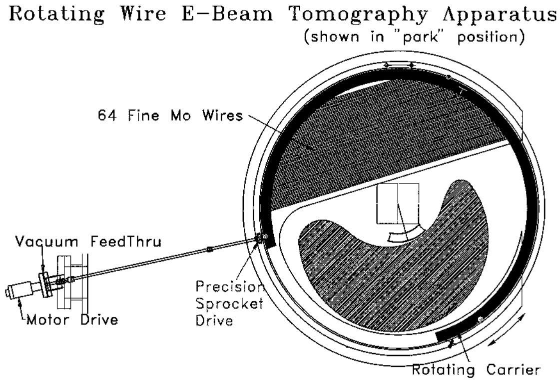

FIG. 1. Simplified drawing of the wire grid apparatus installed at $\Phi=85°$. The grid is shown in "park" position. The plasma is represented by the hatched bean-shaped region.

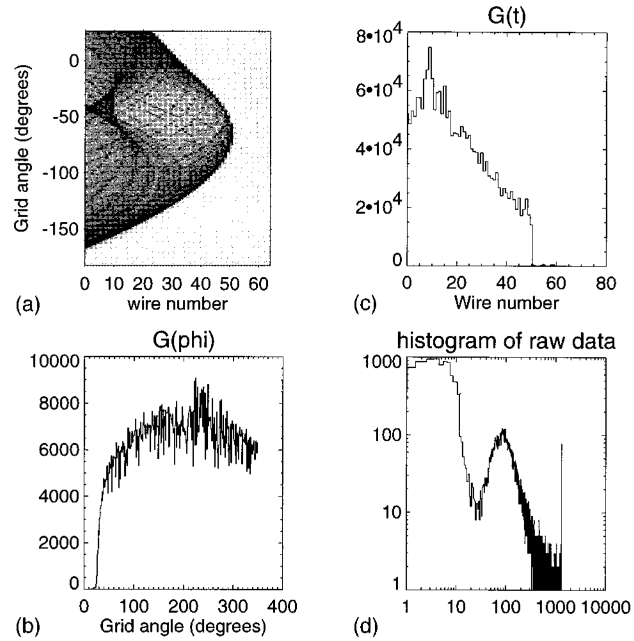

FIG. 2. (a) image representation of raw data for an outer surface of the standard configuration. Data summed over (b) wire, (c) angle, and (d) histogrammed. 350 steps of 0.6° recorded, with significant signals in 50 wires.

A sprocket drive on the wheel perimeter allows the use of surface-hardened precision gear pins with minimum contact area to allow unlubricated operation under vacuum. For angular precision, the drive is directly coupled through a 0.35 Nm rotary feedthrough (the major source of a total backlash of $\pm 5°$) to a 0.7 Nm stepping motor, which is operated in four-phase analog microstepping mode (1500 steps/rev) for maximum resolution and minimal vibration without torque loss. A contact brushing the drive pins allows the angular position of the wheel to be monitored, independently of the drive backlash. The *V* groove was lightly lubricated with silicon vacuum grease, and the motor acceleration was limited, to avoid stepping motor slippage caused by static friction and inertia. Signals leave the carrier in fine teflon insulated wires grouped loosely inside a common braided shield, traveling over guide rollers to a multipin electrical feedthrough. Each of 64 channels of signal processing consists of a high gain current to voltage convertor 10^7 V/A (or 10^6, 10^8) followed by a two pole active low pass filter at 300 Hz (or 3/30 Hz), optimized for very low frequency noise ($I_{\mathrm{equiv.rms}}<6\times 10^{-13}$ A/$\sqrt{\mathrm{Hz}}$). Analog multiplexers feed all channels through an isolation amplifier into a single analog to digital convertor (ADC), and the remainder of connections are binary opto-isolated lines (six channel select, four limit/control switches), allowing high voltage isolation of the interface.

The electron gun is a thorium-coated tungsten filament (0.3 mm diam) in a stainless steel tube with a beam exit hole of 0.7 mm, operated at 1.4 A to produce a beam current of 1 μA out of a total 8 μA emission.

III. RESULTS

The raw data in Fig. 2 is shown as a sinogram, truncated to half-cycles because of the limited angular scan ~210°. Each half-cycle represents a puncture point. The data presented are from three different surfaces of the standard configuration of H-1,[6] (10, 1, 0, 0.44, 0.22), and one other configuration (Fig. 5).

For basic resolution tests, a simple case with just one transit is investigated, because the transit number is well known, and there is no possibility of interception of the electron beam by other wires (shadowing) on earlier transits. Figure 3 shows the collected current as a function of the perpendicular distance from wire 58 to the deduced beam centroid as the wire scans through the beam. This wire is the furthest wire from the wheel center that passes through the puncture (the "tangential" wire) so the cross section is mapped out in detail, because the angular motion causes the wire to move very slowly in the direction perpendicular to that wire. Traces from wires closer to the center will be less detailed, and in some cases, signals on wires very near the

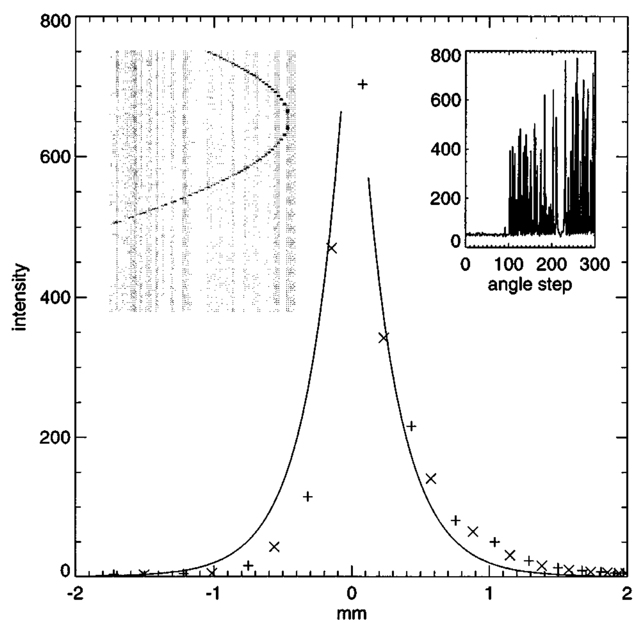

FIG. 3. Example of a simple beam profile for single transit data showing a resolution of 0.4 mm FWHM. $\times$ and $+$ represent data from the peaks above and below the symmetry point. An exponentially decaying function is shown for comparison, $\exp(-3.8|x|)$, raw data, and summed current are inset.

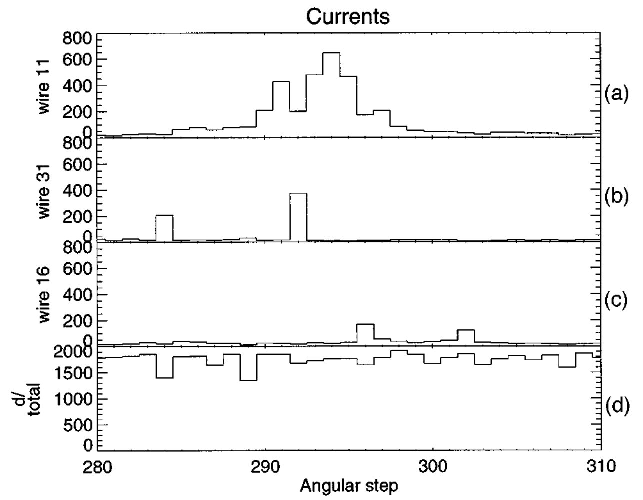

FIG. 4. Shadowing example (a) current in wire 11, (b), (c) the currents in 31 and 16 shadowing the wire 11 current, and (d) the approximately constant sum over all wires.

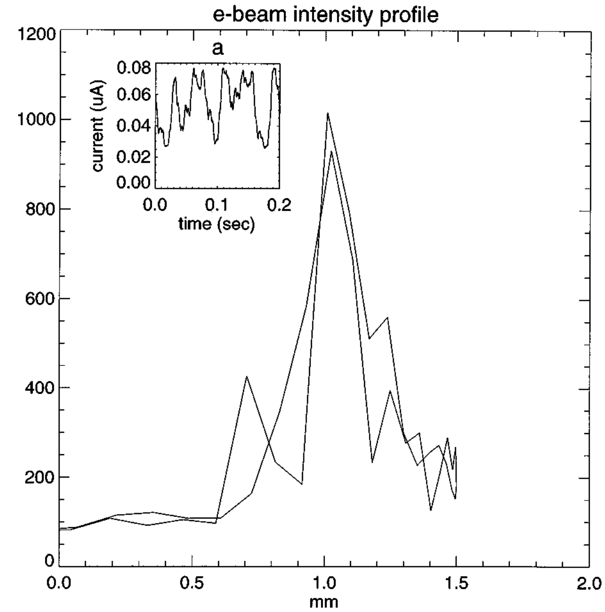

FIG. 5. Beam profile in the presence of small current ripple. H-1 config 10/1/0.037/0.44/0.22.

center will be undersampled to the extent that no peak is seen at all. It can be seen from Fig. 3 that the overall resolution is about 0.4-mm full-width half-maximum (FWHM). The repeatability and lack of noise in the data is evident from the near-perfect interleaving of the two peaks that occur either side of the *symmetry point* (when a radial line perpendicular to the wires passes through the beam puncture being considered). The observed resolution is better than the collimating aperture of the electron gun, indicating that for these conditions, the filament is partially eclipsed by the aperture along the direction of the magnetic field lines.

A more typical profile is shown in Fig. 4, from a surface which has at least 19 clear transits, and "shadowing" of wire by two other wires in previous transits is clear. In other cases, the shadow is a similar size to the peak, in which case the peak height is simply reduced.

The effect of beam jitter is shown in Fig. 5. This shows a similar resolution, but the scatter in data on either side of maximum is attributed to a tiny periodic motion in the position of the beam caused by a small ripple in the magnet current ($\delta I/I \sim 1\times10^{-4}$). A time record of current collected by a wire on the shoulder of the peak is shown inset, showing modulation at the generator rotation frequency, 12.5 Hz. Normally self-similarity of currents in the standard configuration (in which there are no shunts present to alter current ratios) prevents this phenomenon, but for Fig. 5, the helical current is adjusted by an uncompensated resistive shunt, so the ripple is slightly dephased in the helical winding, relative to all other currents (leading to an effective $\delta I/I \sim 3\times10^{-5}$).

This illustrates the sensitivity of this apparatus to very small changes in configuration, and the usefulness of the time-dependent output of the apparatus. Because the helical current strongly affects the rotational transform, the jitter effect grows with transit number, and can be used to identify the transit sequence number, for absolute determination of rotational transform.

"Open" trajectories may be detected by monitoring the total current summed over all wires (including the shield return of the electron gun). When a field line ends by hitting the vessel wall, the total collected current shows a sharp drop when the beam passes between wires, and is not collected by the array. This is evident in the sum data inset in Fig. 3, and by comparison to a closed surface in Fig. 2, where the total current is modulated much less deeply.

A full analysis of the tomographic inversion of the data to produce an image of the punctures is beyond the scope of this article. The dataset is relatively sparse in one dimension (impact parameter), and the attenuation due to shadowing is a perturbative process, particularly when the shadowing is well defined as in Fig. 4. A simple multiplicative arithmetic reconstruction technique (ART)[8] inversion is shown in Fig. 6, but the resolution falls well short of the demonstrated resolution of the data (0.4 mm).

Transparency is determined by the geometric transparency of the grid (96%) and the detailed trajectories of the electrons in the vicinity of individual grid wires. The background gas pressure limits the realizable transparency by causing gradual energy loss and pitch angle scattering of electrons. In the H-1 heliac, such scattered electrons are trapped once their pitch angle exceeds 20°–40°, causing a loss in collected current and build up of space charge which diffuses and eventually is collected by the wires as a broad background feature (the gray area in Fig. 2). For these results, the total pressure was 2×10^{-7} Torr (50% H_2O, 30% N_2), implying an upper limit on the mean free path of 200 transits from pitch-angle scattering. Scaling of experimental data at a pressure of 1×10^{-5} Torr, where only 1 transit was observed indicates a limit of 50 transits.

The observed $1/e$ attenuation distance was about 20 transits at best, with typically up to 40 transits visible in the raw data. This is about 1/2 the value expected from the geometric transparency, and is qualitatively consistent with the combined effect of background gas and geometric transparency.

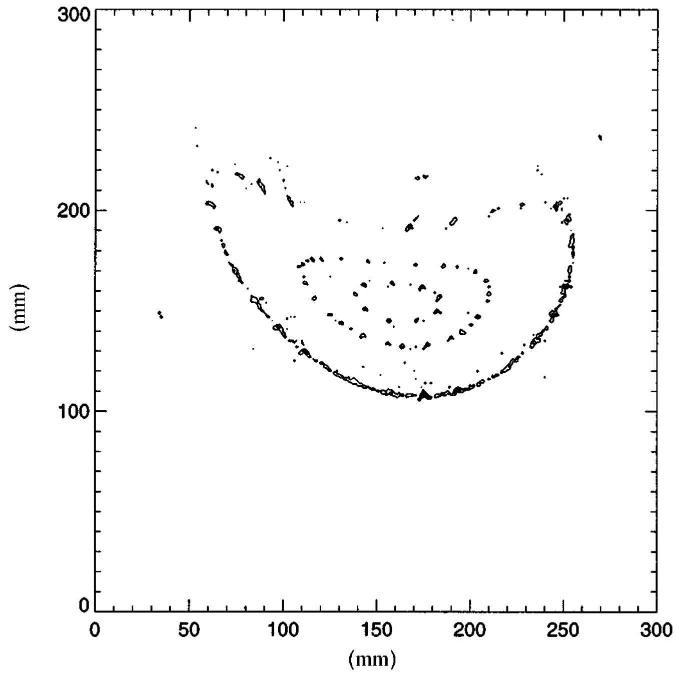

FIG. 6. Simple tomographic reconstruction of the data of Fig. 2 and two inner surfaces superimposed.

The possibility of improving on the geometric limit is discussed later.

IV. DISCUSSION

The major compromise in the design of this apparatus is the tradeoff between tomographic imaging resolution and transparency by varying the number of wires. The information content of a smaller array of wires cannot be recovered simply by sampling more angles. Typically the tomographic ($1/r$ ''spokelike'') artifacts become much more pronounced.

Instead, it may be possible to retain a large number of wires and overcome the geometric transparency limit by biasing the grid slightly in *repulsion*. This would cause many of the trajectories that would have intercepted the wires to deviate slightly, but still allow others (with very low impact parameter) to hit the wires. A limitation of this ''electrostatically variable transparency'' technique is that the radius of curvature of the deviation from the orbit from the field line is not negligible compared to the Larmor radius of the electron's parallel motion ($v_\parallel/\omega_c$), so the first adiabatic invariant μ will not be conserved and pitch angle scattering will occur, causing attenuation and diffusion as discussed above. Preliminary tests indicate some improvement, but it is likely that lower energies, background pressures, and higher magnetic fields will be required to demonstrate this clearly.

In summary, the high resolution and accuracy of the apparatus make it well suited to detailed point-by-point comparison of mapped surfaces with computations, typically performed in the process of evaluating magnetic geometry and the effect of error fields. The simple tomographic inversion presented here illustrate the potential for medium-quality imaging of surfaces, and it is expected that refinement of the inversion algorithms will improve the image quality to more closely mirror the resolution of the raw data.

ACKNOWLEDGMENTS

The authors are grateful for discussions with D. Rudakov, and technical assistance from E. Wedhorn, R. Davies, R. Cruikshank, R. Kimlin, and G. Hoecherl, and special acknowledgements are due to the excellence in design and craftsmanship of H. Zeilinger, J. Wach, and N. Trama, without which this apparatus would not have been possible. Computer time on the Fujitsu VP2200 supercomputer was provided by the ANU Supercomputer Facility.

[1] B. D. Blackwell, J. Howard, and R. B. Tumlos, Rev. Sci. Instrum. **63**, 4725 (1992).
[2] R. M. Sinclair, J. C. Hosea, and G. V. Sheffield, Rev. Sci. Instrum. **41**, 1552 (1970).
[3] R. Jaenicke, E. Ascasibar, P. Grigul, I. Lakicevic, A. Weller, M. Zippe, H. Hailer, and K. Schworer, Nucl. Fusion **33**, 687 (1993).
[4] R. J. Colchin, S. C. Aceto, A. C. England, R. C. Isler, M. Murakami, D. A. Rasmussen, T. Uckan, J. B. Wilgen, and J. J. Zielinski, Nucl. Fusion **33**, 323 (1993).
[5] T. Y. Tou, B. D. Blackwell, and L. E. Sharp, Rev. Sci. Instrum. **62**, 1149 (1991).
[6] M. G. Shats, D. L. Rudakov, B. D. Blackwell, L. E. Sharp, R. B. Tumlos, S. M. Hamberger, and O. I. Fedyanin, Nucl. Fusion **34**, 1653 (1994).
[7] S. M. Hamberger, B. D. Blackwell, L. E. Sharp, and D. B. Shenton, Fusion Technol. **17**, 123 (1990).
[8] R. B. Tumlos, Ph.D. thesis, ANU (1994).